Nuclear Engineering and Design 446 (2026) 114632

Contents lists available at ScienceDirect

Nuclear Engineering and Design

journal homepage: www.elsevier.com/locate/nucengdes

Simulation of flow field characteristics around longitudinally staggered variable-curvature helical coil bundles

Zhao Xijun [a,b], Qin Kaiwen [a,b], Tang Xiaobin [a,b,*]

[a] Department of Nuclear Science and Technology, Nanjing University of Aeronautics and Astronautics, Nanjing 211106, China
[b] Key Laboratory of Advanced Nuclear Technology and Radiation Protection, Ministry of Industry and Information Technology, Nanjing 211106, China

ARTICLE INFO

Keywords:
Steam generator
Variable-curvature helical coil
Coil bundle
Longitudinal staggered arrangement
Turbulent mixing

ABSTRACT

In advanced heat exchanger systems such as steam generators, enhancing shell-side heat transfer efficiency while managing flow resistance remains a critical engineering challenge. This study proposes a novel variable-curvature helical coil bundle with longitudinal staggered arrangement to improve turbulent mixing. A numerical study was conducted on the shell-side flow field structure of a five-layer helical coil bundle. The distributions of velocity, vorticity, Q value, and turbulent kinetic energy were analyzed. The results showed three distinct regions in the outside flow field of the five-layer helical coil bundle: A (inline arrangement), B (staggered), and C (mixed arrangement). Region B achieved a 72 % higher Nusselt number (Nu = 7.16) than Region A (Nu = 4.16). The variable-curvature design reduced flow blockage by 34 %. This study offers theoretical support for the research and design of novel heat exchange tubes for steam generators.

1. Introduction

Helical coil heat exchangers are characterized by their compact structure, high spatial efficiency, efficient heat transfer, and excellent thermal expansion self-compensation. These advantages have led to their adoption in various nuclear reactors, including the Integral Reactor Innovative and Secure, high-temperature gas-cooled reactor with pebble-bed modules, sodium-cooled fast reactor (Superphénix), small modular reactors (NuScale, ACPR50S), and marine pressurized water reactors (Otto Hahn) (Ding et al., 2020; Lee and Hassan, 2020; Rivas and Rojas, 2016; Namhyeong Kima, 2020; Markus Esch, 2012). The helical steam generator is a critical technology for nuclear energy advancement (Qizhen, 2015).

Since the invention of helical coil heat exchangers in 1895 (Wei et al., 2022); extensive numerical simulations (Lee and Hassan, 2020; Yildiz et al., 2018) and experimental studies (Zhao and Che, 2012) have been conducted on helical coils. Research has focused on adjusting structural parameters (coil curvature (Moawed, 2011; Yoo Geun-Jong, 2012); diameter (Al-Hasan et al., 2012), pitch), changing coil structural shapes (elliptical flat tubes (Bishara, 2013), helical coils, cross-twisted tubes, square-section twisted tubes, and helically corrugated tubes, etc.), and surface modifications (increasing surface threads, ribs (Wang et al., 2023), corrugations, and grooves (Kunwer et al., 2020); etc.). Gu (Hongfang et al., 2000) studied the effects of changing in the angle or quantity of V-shaped grooves outside the tube bundle on the variation of the condensation heat transfer coefficient. Other researchers have attempted tried to use rectangular (Wang et al., 2021) or elliptical coil windings to improve the heat and mass transfer effects (Miao Gui, 2016). However, most methods assume constant curvature, neglecting its impact on heat transfer (Mori and Nakayama, 1967; Mori, 1967).

For shell-side flows, traditional in-line helical bundles cause flow blockage due to small longitudinal spacing (Beale and Spalding, 1999), reducing turbulent mixing. As shown in Fig. 1, staggered arrangements mitigate this. Staggered tube bundles universally achieve superior heat transfer performance compared to in-line arrangements across circular, elliptical, and helical geometries (Kwak et al., 2003; Linkai, 2017), primarily due to enhanced turbulent mixing (Herchang et al., 2002). Double-staggered configurations provide optimal heat transfer enhancement (Jiang et al., 2019), with specific pitch ratios further amplifying this advantage (Paul et al., 2007), though at the cost of elevated pressure drops relative to in-line layouts (Moreno and Sparrow;

Abbreviations: CFD, computational fluid dynamics; D, diameter; HCSG, helical-coil steam generator; HOTSG, helical coil steam generator; k, turbulent kinetic energy (J/kg); LES, large eddy simulation; OHSG, once-through steam generator; P, pressure (Pa); PIV, particle image velocimetry; RMS, root mean square; SST, shear stress transport; S, strain rate tensor (s); Tr, trace of the matrix; TKE, turbulence kinetic energy (J/kg); UDF, user-defined function; Re, Reynolds numbers.

* Corresponding author at: Key Laboratory of Advanced Nuclear Technology and Radiation Protection, Ministry of Industry and Information Technology, Room B224, Nanjing 211106, China.
E-mail address: tangxiaobin@nuaa.edu.cn (T. Xiaobin).

https://doi.org/10.1016/j.nucengdes.2025.114632
Received 21 June 2025; Received in revised form 27 October 2025; Accepted 20 November 2025
Available online 27 November 2025

Nomenclature

Greek Symbols	Definition (Units)
ε	turbulent dissipation rate (m^2/s^3)
ν	velocity (m/s)
ν	kinematic viscosity ($N{\cdot}s/m^2$)
ν'	kinematic viscosity(y-axis) (m/s)
μ'	turbulent fluctuating velocity(x-axis) (m/s)
ρ	density(kg/m^3)
ω'	turbulent fluctuating velocity(z-axis) (m/s)
Ω	vorticity tensor (1/s)
Q	Q criterion ($1/s^2$)

Gharbi et al., 2015).

This study pioneers a novel variable-curvature helical coil design featuring continuous curvature modulation (Fig. 3), implemented in a five-layer bundle with longitudinal staggered arrangement. Through advanced CFD analysis employing the SST-ω model (Nianben et al., 2017; Asian, 2016), we quantify three distinct flow regimes (A: in-line, B: staggered, C: hybrid), revealing a 72 % enhancement in Nusselt number (Nu = 7.16) within the staggered region (B) compared to conventional in-line configurations (Region A, Nu = 4.16).

2. Helical coil bundles in staggered arrangement

Based on the above literature review and inspiration, this study proposes a new improvement method for helical coil tubes and bundles. This section introduces a variable-curvature helical coil tube and a multiple-layer helical coil bundle.

2.1. A variable-curvature helical coil tube

A new variable-curvature helical coil tube design, featuring periodically and longitudinally alternating curvature (Zhuang et al.), was developed. Potential issues of discontinuous curvature during grid partitioning, such as asymmetric cross-sections and data distortion, were mitigated by this single-root structure.

The construction began with a quarter-ellipse (190 mm long axis, 140 mm short axis) joined smoothly to a quarter-circle (140 mm radius) in the XY plane. Matching slopes and smooth curvature were maintained at the joining point. This flat shape was then moved along a spiral path with 200 mm spacing to create the quarter-coil piece shown in Fig. 2. The piece was turned three times at 90-degree steps and shifted vertically. Three identical pieces were connected to build the full coil section displayed in Fig. 3. The top view showed a clear spiral shape starting from the center, while the front view presented the complete form.

2.2. Five-layer helical coil bundles in staggered arrangement

The configuration of eight helical coils with variable curvatures was obtained by performing seven rotations at 22.5°-intervals and translating along the *Z*-axis by 47 mm (Fig. 4). Subsequently, a structure of five layers of helical coils with variable curvatures was generated by adjusting the parameters outlined in Table 1 and repeating the above operation (Fig. 5).

In conventional constant-curvature helical coils, the distance between the flow and the central axis of the coil bundle is constant. However, in helical coils with variable curvatures, this distance oscillates periodically with the flow (Fig. 6). Each cycle corresponded to 1/4 of the flow path (750 mm).

3. Simulation method

3.1. Mesh configuration

The numerical simulations in this study were performed using the commercial CFD software ANSYS Fluent (v2022 R1). The quality and number of meshes is an important factor in numerical accuracy. Therefore, the model was divided into meshes with the numbers of 1.5 million, 2.45 million, 3.55 million, 4.5 million and 5.0 million, respectively. A mesh independence study was conducted by comparing the area-weighted average velocity at the outlet for different mesh sizes, as summarized in Table 2. The results show that beyond 3.55 million cells, the variation in outlet velocity is less than 2 %, indicating that mesh independence is achieved. Therefore, the model with 3.55 million cells was selected for further numerical simulations to ensure accuracy while maintaining computational efficiency. Fig. 7 illustrates the results of polyhedral mesh generation, mesh independence verification was conducted to achieve optimal simulation performance. When 3.55 million meshes were generated, the velocity flow field was more symmetric and stable. Considering the effect of mesh number on operation speed and simulation accuracy the model with 3.55 million meshes in the computational domain was selected for further numerical simulation.

3.2. Boundary and initial conditions

A rectangular flow field computational domain was selected (Fig. 8).

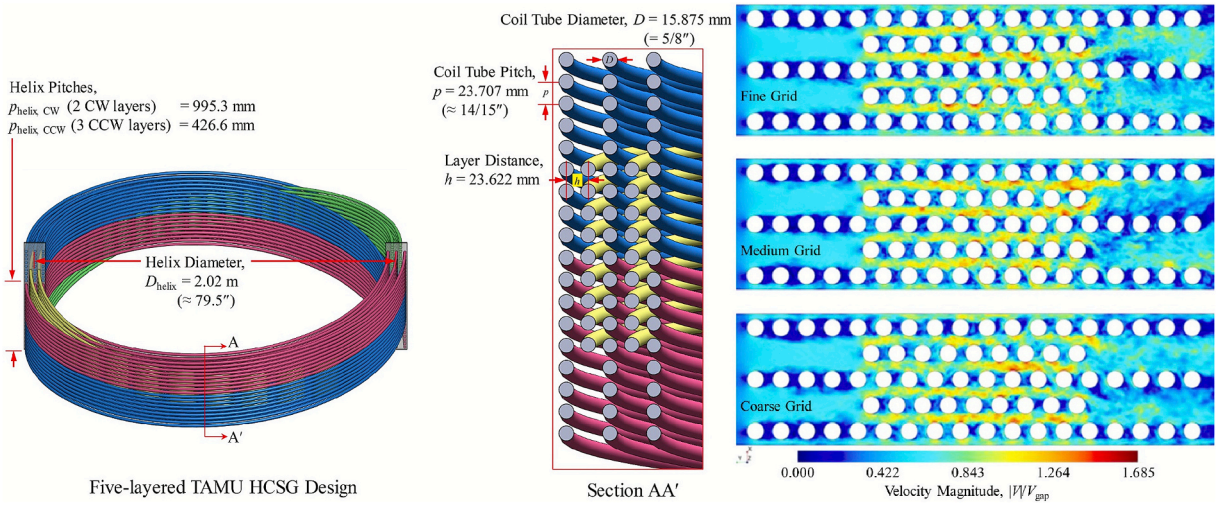

Fig. 1. Speed distribution of spiral coil tube bundle in five-layer helical coil steam generator for advanced small modular reactor design (Lee and Hassan, 2020).

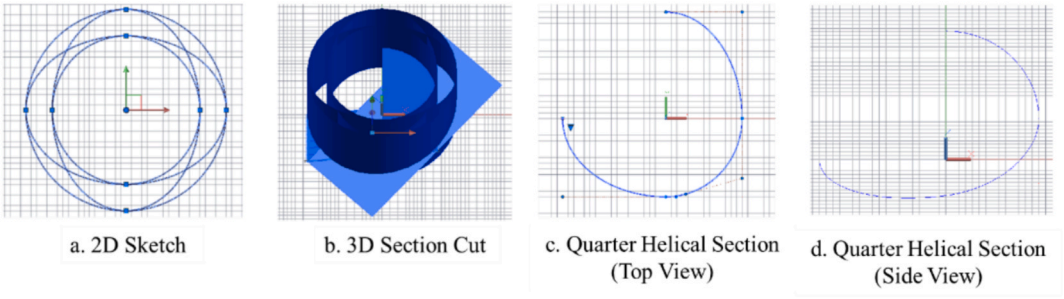

Fig. 2. Diagram for drawing a helical line segment.

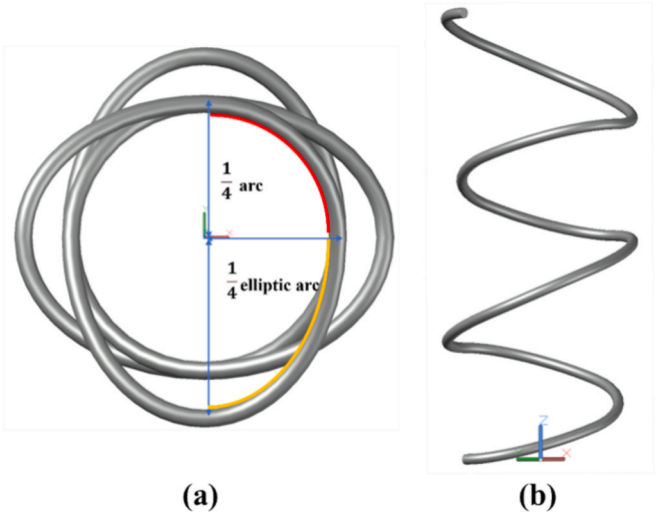

Fig. 3. Schematic of a variable-curvature helical coil tube: (a) top view; (b) side view.

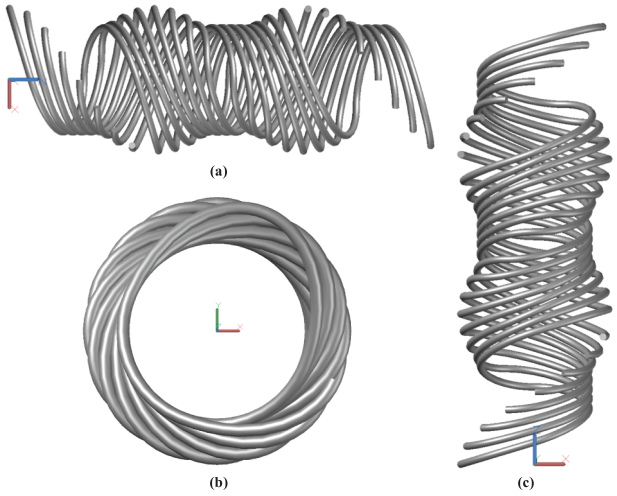

Fig. 4. Structure of a single-layer variable-curvature helical tube bundle: (a) side view of the vertically arranged bundle; (b) top view of the vertically arranged bundle; (c) elevation view of the horizontally arranged bundle.

The dimensions of the computational domain were determined based on established best practices for cross-flow simulations over tube bundles. The upstream length was set to 5 hydraulic diameters (5D) ahead of the first tube row to ensure the development of a uniform inlet flow profile. The downstream length was extended to 10D beyond the last tube row to allow for complete flow development and pressure recovery, thereby

Table 1
Structural Parameter of the helical coil bundle.

Number of layers	Minor axis (mm)	Major Axis (mm)	Pitch (mm)	Axial distance (mm)	Outer diameter of the pipe (mm)	Inner diameter of the pipe (mm)
1	140	190	200	47	19	3
2	165	215	200	47	19	3
3	190	240	200	47	19	3
4	215	265	200	47	19	3
5	240	290	200	47	19	3

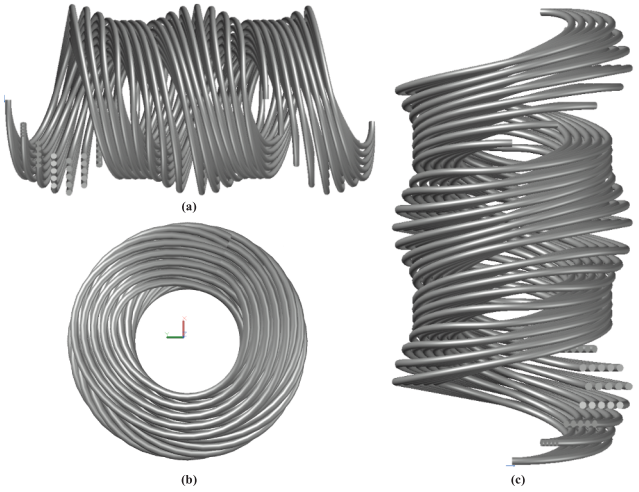

Fig. 5. Structure of a five-layer variable-curvature helical coil bundle: (a) side view of the vertically arranged bundle; (b) top view of the vertically arranged bundle; (c) elevation view of the horizontally arranged bundle.

avoiding any reverse flow influence at the pressure-outlet boundary. Although the full helical coil bundle is complex, its arrangement exhibits inherent circumferential periodicity. Therefore, instead of modeling the entire annulus, a narrow, representative rectangular was used. This sector fully spans the radial extent of the bundle, encompassing all three characteristic regions (A, B, and C). The two side boundaries of this sector were treated as periodic boundary conditions, which mathematically replicates the conditions of a full, continuous environment while significantly reducing computational cost. SST k-ω turbulence model was applied. An inlet velocity of 0.5 m/s was applied at the inlet surface. A pressure of 8 MPa was applied at the outlet boundary to simulate the operating conditions of a high-temperature gas-cooled reactor. The gas flow direction was from top to bottom, and adiabatic conditions were set around it. The minimum convergence criterion was 10^{-6} for the continuity equation, velocity and turbulence quantities and 10^{-8} for the energy equation.

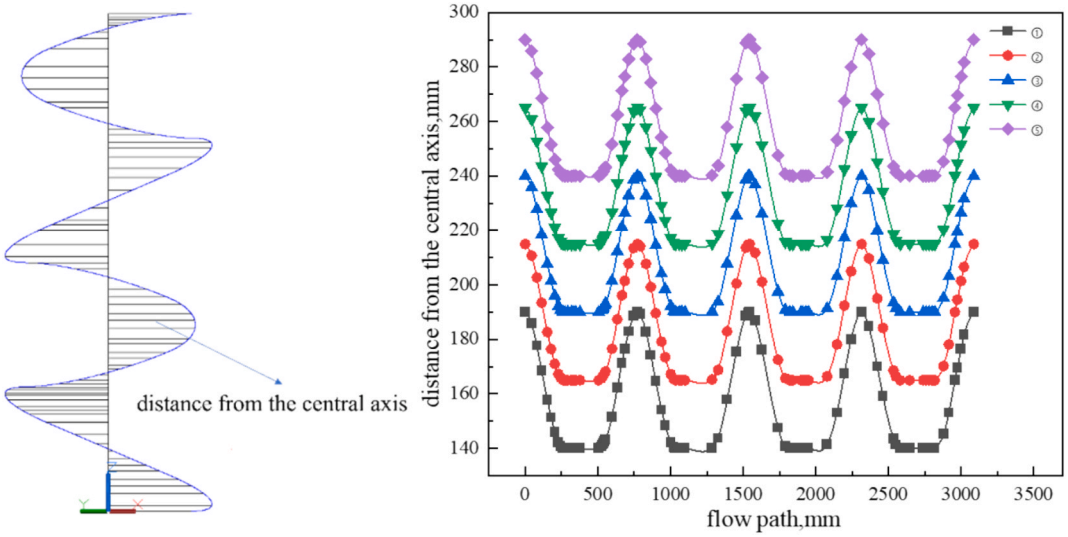

Fig. 6. Distance of the coil tube along the flow path to the central axis.

Table 2
Mesh independence study results.

Number of cells (million)	Outlet velocity (m/s)
1.5	0.432
2.45	0.451
3.55	0.457
4.5	0.457
5.0	0.457

3.3. Numerical discretization

The governing equations for continuity, momentum, and energy were discretized and solved using the finite volume method (FVM), with the pressure–velocity coupling achieved through the SIMPLE algorithm. The spatial discretization schemes were applied as follows: the Least Squares Cell Based method was used for computing the gradient, the PRESTO! scheme was selected for pressure interpolation, and the Second Order Upwind scheme was adopted for the discretization of momentum, turbulent kinetic energy, specific dissipation rate, and energy equations. These schemes were chosen to ensure a good compromise between computational accuracy and stability for the complex flow geometry under investigation (Fig. 10).

3.4. Turbulence model

As discussed in the Introduction section, the characteristics of the flow across the tube row of coil bundles are inverse pressure gradient, flow separation and vortex shedding. Menter (Menter, 1994) and Atlar et al. (Ünal et al., 2010) studied the commonly used turbulence models such as Spalart-Allmaras model, realizable k-ε model and SST(shear-stress transport) k-ω model. The conclusions show that the SST k-ω model can better predict such flows. Qin Yangjia (Yangjia et al., 2023) employed the SST k-ω model to simulate the flow and heat transfer characteristics outside staggered tube bundles undergoing crossflow. Similarly, Guo Jun (Jun and Xun-Ming, 2015) utilized the SST-ω model to conduct numerical simulations of the flow and heat transfer in helical tube bundles and successfully obtained information on the flow field and temperature field for crossflow across complex helical tube bundles. These articles show that SST-ω shows the best agreement with the experimental results, so the SST-ω model is used in this study.

To validate the numerical methodology, a comparative study was

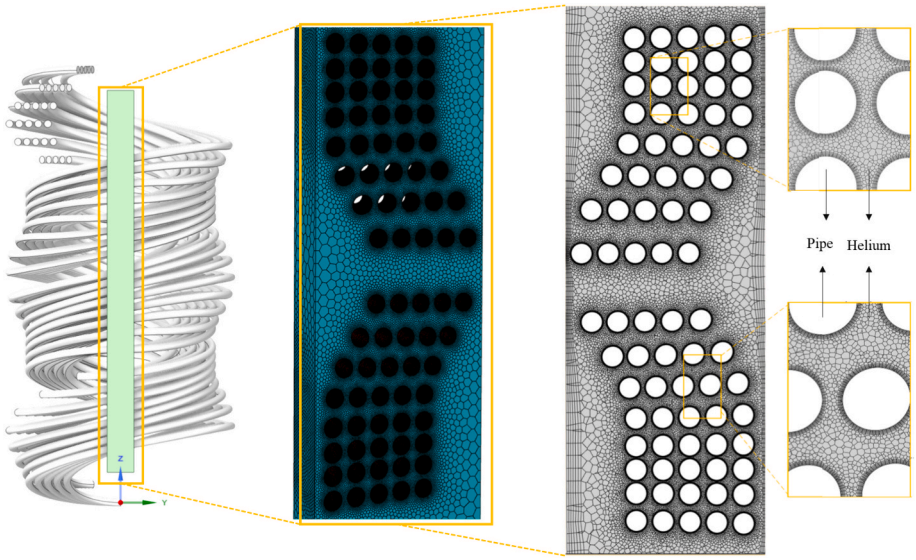

Fig. 7. 3.55 million grid cells and their details.

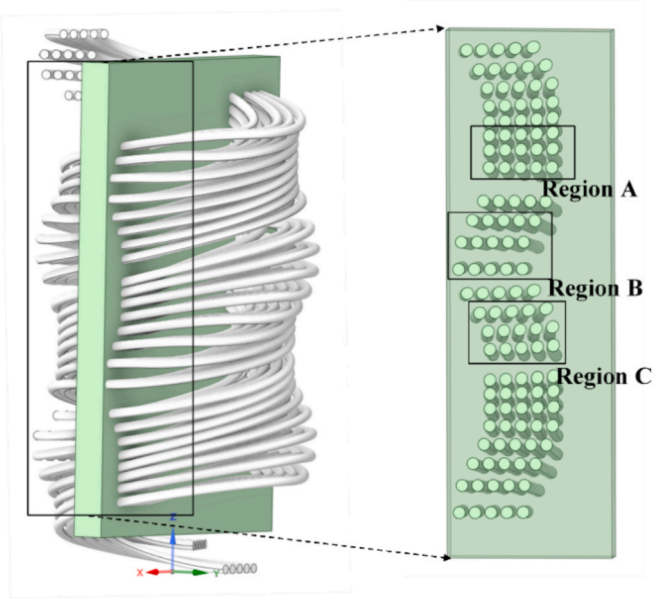

Fig. 8. Computational domain and definition of the analysis regions.

conducted by replicating the simulation setup previously employed by Lee and Hassan (Lee and Hassan, 2020). The dimensionless velocity profiles were compared at the same downstream location, identified as L06 in the reference study. Excellent agreement was observed in the overall distribution pattern between the two investigations. A slight over-prediction of approximately 8 % was noted in the peak region when using the SST k-ω model (Fig. 9). This discrepancy was considered consistent with established methodological differences between the approaches. The Large Eddy Simulation methodology directly resolves large-scale turbulent fluctuations, while the RANS-based SST k-ω model's eddy-viscosity hypothesis tends to dampen such fluctuations, producing a more time-averaged flow field. The level of deviation was found to fall within the expected range for this type of cross-validation study, thereby confirming the reliability of the present numerical approach for capturing the essential flow physics in helical coil configurations.

4. Results and discussion

This section first provides a general description of the flow field outside a helical coil bundle. A detailed analysis of Regions B and C was then conducted. Finally, the turbulent mixing levels were compared.

4.1. General description of outside flow field

Three distinct flow regimes (A, B, C) were identified based on tube arrangement patterns. Region B (staggered) and Region C (hybrid) exhibited oblique velocity vectors and elevated Q-criterion vorticity (>0), indicating rotational-dominant flow structures. In contrast, Region A (in-line) showed suppressed vorticity and low-velocity zones due to axial flow alignment and reduced lateral mixing. Subsequent analysis was focused on Regions B and C where enhanced turbulent mixing was observed.

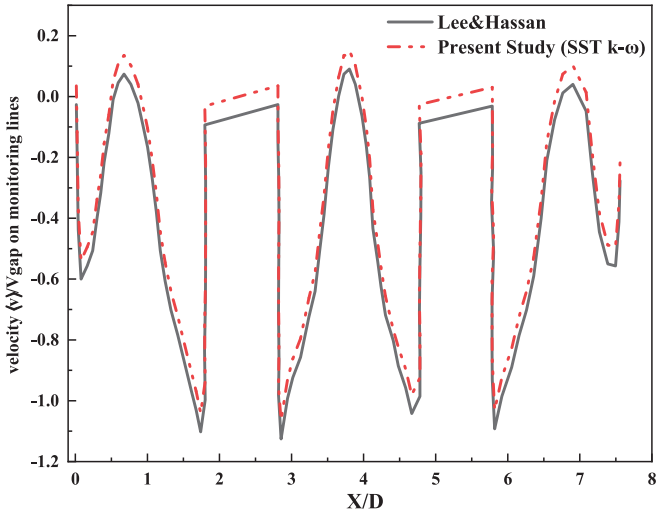

Fig. 9. Comparison of dimensionless velocity profiles ($<v>/V_{gap}$) at the same downstream location (L06) between the present SST k-ω simulation and the LES results from Lee & Hassan (Lee and Hassan, 2020).

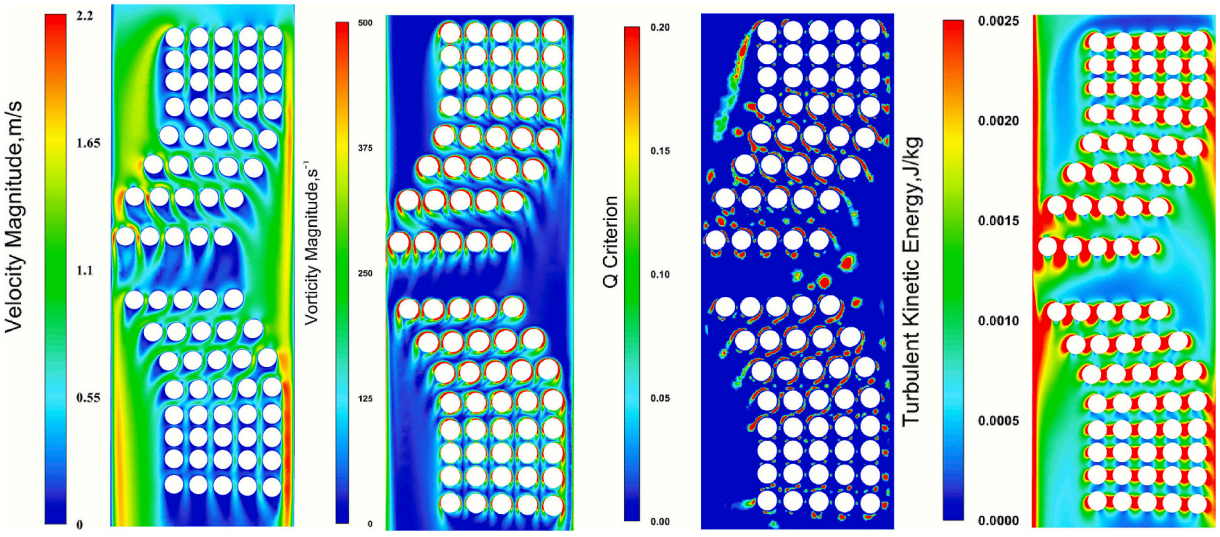

Fig. 10. Velocity, vorticity, Q value, turbulent kinetic energy of each Region.

4.2. Distribution characteristics of flow field in region B

4.2.1. Velocity distribution

Transverse flow separation was induced by variable curvature (Fig. 11), evidenced by leftward-shifted velocity peaks in B1–B5 (Fig. 12). Downstream (B6–B10), velocity attenuation was accompanied by a 15 % increase in mean flow velocity, attributed to vortex shedding from curved segments. This acceleration enhanced convective heat transfer by thinning thermal boundary layers.

4.2.2. Vorticity and Q criterion distribution

As shown in Figs. 13 and 14, in Region B, strong vortical structures ($Q > 0$) were formed at tube crowns, while wake regions exhibited negative Q-values indicative of strain-dominated flow. Vorticity magnitude increased by approximately 40 % at variable-curvature transitions (B7 vs. B1 in Fig. 15), demonstrating curvature-induced vortex enhancement. The selection of positions B1 and B7 for comparison is strategic: B1 captures the flow state at the onset of curvature variation, while B7 represents a downstream location where curvature-induced vortex shedding reaches its peak intensity. This comparison effectively highlights the evolution and enhancement of vortical structures due to the variable-curvature design. This mechanism promoted turbulent mixing and thermal transport.

The formation of strong, coherent vortex structures ($Q > 0$) at the tube crowns is crucial for heat transfer enhancement. These vortices act as 'mixing agitators', periodically sweeping away the thermally saturated fluid from the tube surface and replacing it with cooler core fluid. This process thins the thermal boundary layer and increases the local temperature gradient, which is the primary driver of convective heat transfer. Furthermore, the oscillation in the distance to the central axis (Fig. 6) in the variable-curvature design creates a pulsating effect that prevents the boundary layer from becoming fully developed, further contributing to the thermal performance.

4.2.3. Turbulent kinetic energy distribution

Peak turbulent kinetic energy (TKE) was localized at the leeward surfaces of the tubes (Fig. 16), coinciding with the flow separation points and shear layers where velocity gradients are most intense. The 22 % increase in TKE from upstream (B1-B5) to downstream (B6-B10) segments, as shown in Fig. 17, is directly correlated with the evolution and periodic shedding of vortices generated by the variable curvature. The staggered arrangement not only enhances turbulence production by promoting more frequent vortex shedding from the tubes but also optimizes its distribution by minimizing flow stagnation zones. This widespread and elevated turbulence level significantly intensifies fluid mixing, which is a primary mechanism for the enhanced convective heat transfer observed in Region B, as it promotes the efficient transport of thermal energy from the tube walls into the bulk flow.

4.3. Distribution characteristics of flow field in region C

4.3.1. Velocity distribution

Oblique flow trajectories were observed without distinct low-velocity zones (Fig. 18). Velocity amplitudes showed periodic fluctuations correlated with curvature variations (Fig. 19). The absence of flow separation resulted in 15 % lower peak velocities than Region B.

4.3.2. Vorticity and Q criterion distribution

As shown in Figs. 20 and 21, a reduction in vorticity magnitude and a significant decrease in the regions of high positive Q-value were observed in Region C, suggesting viscous stress dominance over rotational motion. A critical observation from the Q-criterion contour plot (Fig. 21) is the widespread presence of blue regions, highlighted by red circles, which signify negative Q-values. This pattern indicates that strain-dominated flow structures are pervasive throughout the hybrid arrangement. This hybrid arrangement was characterized by moderate turbulence enhancement but limited vortex coherence, as evidenced by the weaker and less extensive $Q > 0$ structures, compared to Region B.

As shown in Fig. 22, in Region C, a progressive decline of positive Q-criterion values was observed from C1 to C5, culminating in near-zero values at C4. Although the negative Q-values are small in magnitude—so close to zero that they are visually inconspicuous in the line plot—they numerically dominate the majority of the flow field. This trend indicated vortex suppression and viscous stress dominance, which was corroborated by vorticity peaks aligned with tube surfaces in C6-C10. Oblique flow trajectories without flow separation suggested attenuated vortex coherence. The clear and widespread identification of these negative Q regions ($Q < 0$) conclusively confirms that straining motions, rather than coherent vortical structures, govern the hybrid arrangement of Region C. Consequently, heat transfer efficiency decreased due to limited turbulent mixing caused by viscous dissipation overpowering rotational motion. This flow mechanism directly correlates with the intermediate thermal performance of Region C. As quantitatively presented later in Table 4, Region C yielded a Nusselt number of $Nu = 6.55$, which is lower than that achieved in Region B ($Nu = 7.16$).

The intermediate thermal performance observed in Region C can be directly attributed to the attenuation of coherent vortical structures and the concomitant dominance of viscous effects. This is quantitatively evidenced by a pronounced reduction in both the magnitude and spatial distribution of regions exhibiting positive Q-criterion values ($Q > 0$) relative to Region B, signifying a suppression of organized rotational flow. Consequently, the vortex-induced agitation mechanism that promotes efficient thermal boundary layer thinning in Region B is significantly diminished. Heat transfer thus proceeds primarily through molecular diffusion and less intense convective mixing, resulting in the development of a thicker thermal boundary layer. The hybrid arrangement characteristic of Region C therefore represents a flow regime that, while effectively mitigating large-scale flow stagnation characteristic of Region A, fails to produce the vigorous, vortex-enhanced mixing responsible for the superior heat transfer performance achieved in Region B.

4.3.3. Turbulent kinetic energy distribution

As shown in Fig. 23, the turbulent structures in Region C are less coherent compared to those in Region B. This visual evidence of

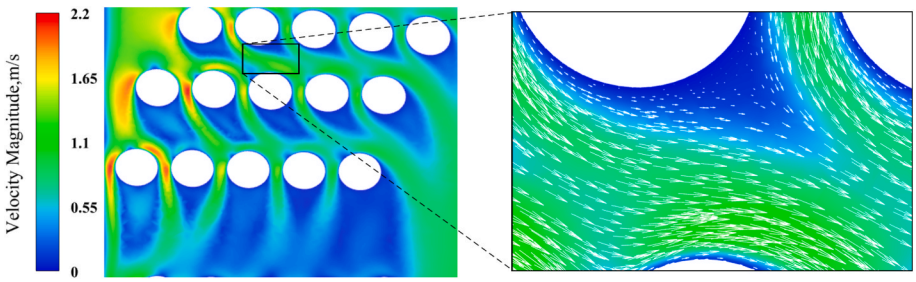

Fig. 11. Velocity contour and local vector in region B.

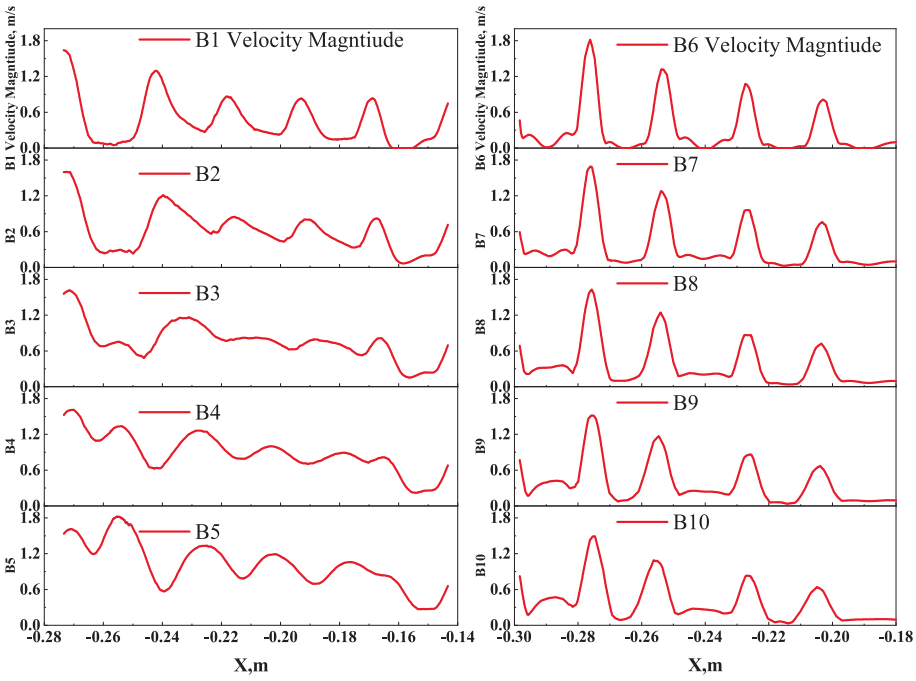

Fig. 12. Comparison of velocity distribution in region B.

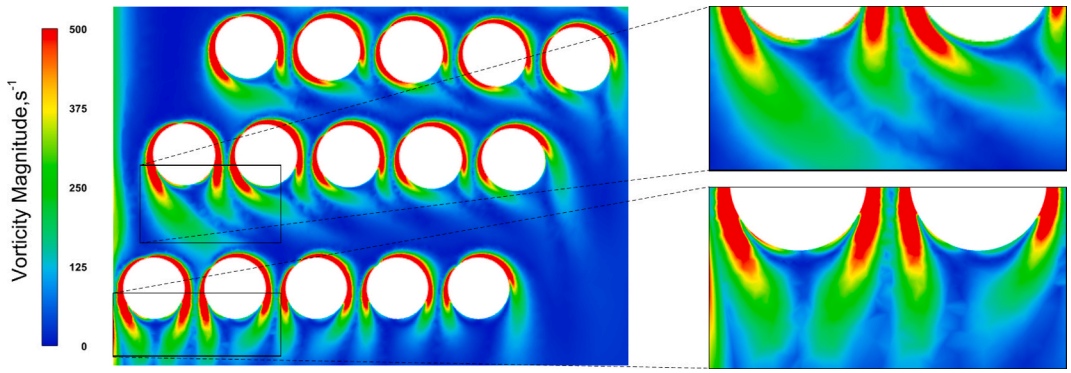

Fig. 13. Vorticity contour in region B.

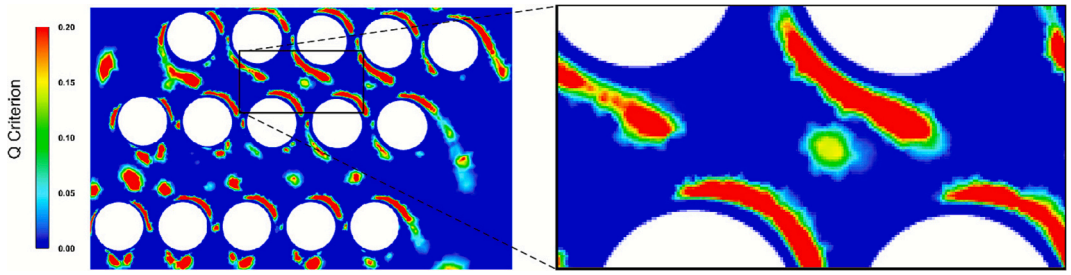

Fig. 14. Q Criterion contour in region B.

underdeveloped flow patterns correlates with the quantitative data in Fig. 24, which confirms that Region C sustains lower levels of Turbulent Kinetic Energy (TKE) and exhibits negligible growth downstream. To enable a fair comparison of the distribution patterns across different physical locations, the transverse position in Fig. 25 has been normalized by the local channel width. This direct comparison of TKE profiles provides definitive validation, demonstrating that the TKE in Region C is not only weaker but also less widespread than in Region B. This consistent evidence across all three figures confirms that the hybrid arrangement of Region C suppresses the full development of turbulence, leading to its inferior TKE performance.

The lower overall TKE in Region C results from dampened turbulent production caused by suppressed vortex shedding. While the localized TKE enhancement at the interfaces provides some mixing benefit, it is insufficient to dominate the global flow field. This results in a flow regime that is neither highly dissipative like Region B nor low-energy like Region A, correlating perfectly with its intermediate pressure drop and heat transfer coefficient. The energy that would have been converted into turbulent kinetic energy for mixing is instead dissipated viscously, which contributes to the flow resistance without equivalently

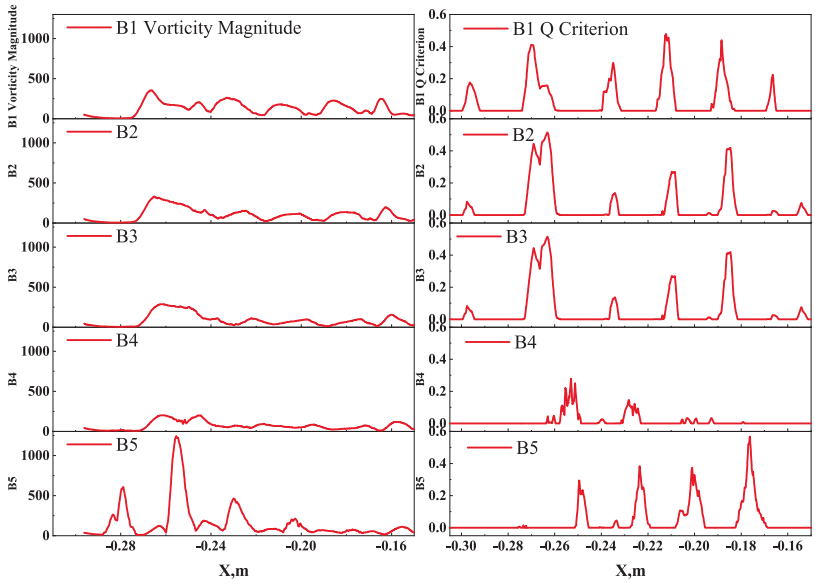

a. B1–B5

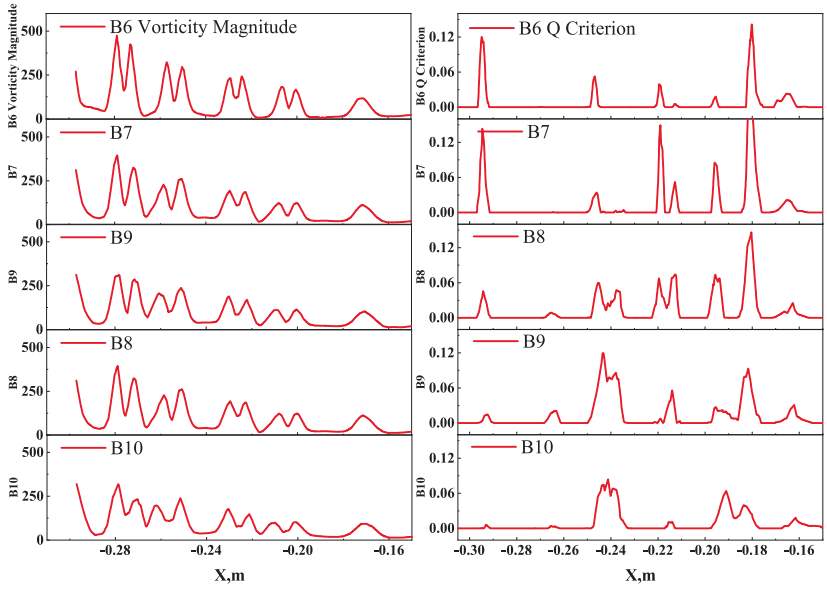

b. B6–B10

Fig. 15. Comparison of vorticity distribution (left) and Q criterion distribution (right) in region B.

enhancing heat transfer.

4.4. Distribution characteristics of three regions

4.4.1. Transverse turbulence velocity comparison

A classical user-defined secondary flow (root mean square of the transverse turbulence velocity, RMS) was chosen as the evaluation criterion to assess the mixing efficiency of the coolant. The specific expression for the secondary flow is given by

$$S = \sqrt{u^2 + v^2} \tag{1}$$

where u and v are the lateral velocities perpendicular to the axial direction.

As shown in Figs. 26 and 27, the RMS value of the lateral turbulent velocity in Region A varied relatively uniformly over the whole area, reaching its maximum in the third row of bundles. This observation indicates a relatively uniform degree of turbulent mixing in Region A, with intense turbulence noted at the third row of bundles, where the peak is highest.

The RMS values of the lateral turbulence velocity in Region B are higher, indicating a more pronounced level of turbulence mixing in Region B compared with Region A. The enhancing effect of the staggered arrangement on turbulence mixing was further confirmed.

Although the RMS values of the lateral turbulent velocity in Region C are relatively small, an upward trend is observed after passing through the variable-curvature section.

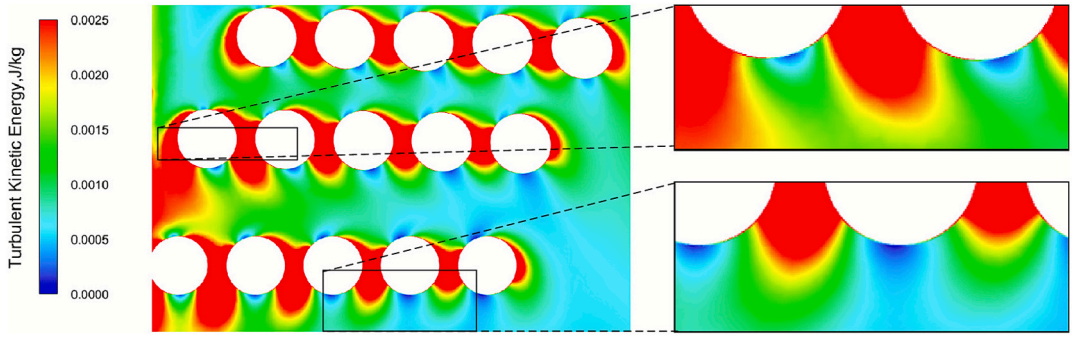

Fig. 16. Turbulence kinetic energy contour in region B.

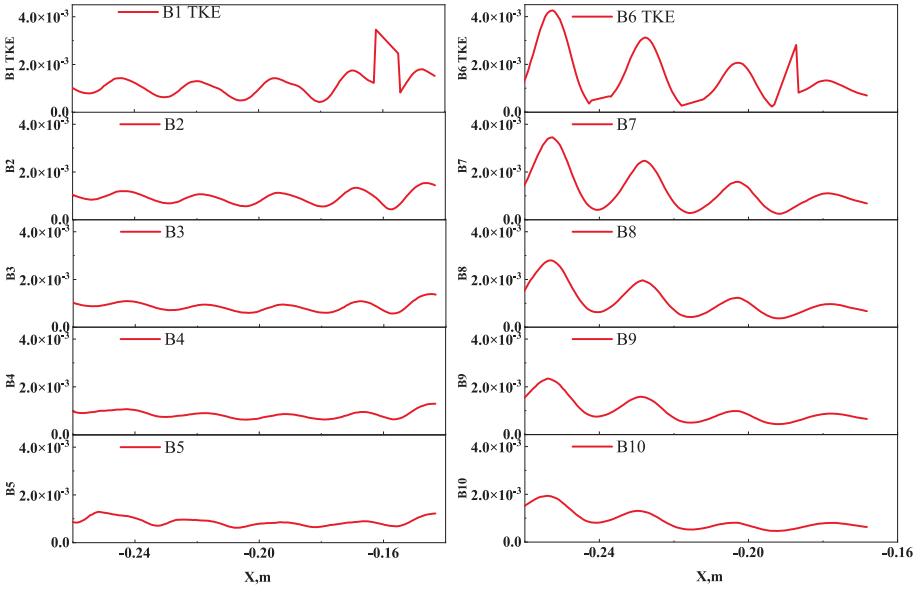

Fig. 17. Comparison of turbulence energy data in region B.

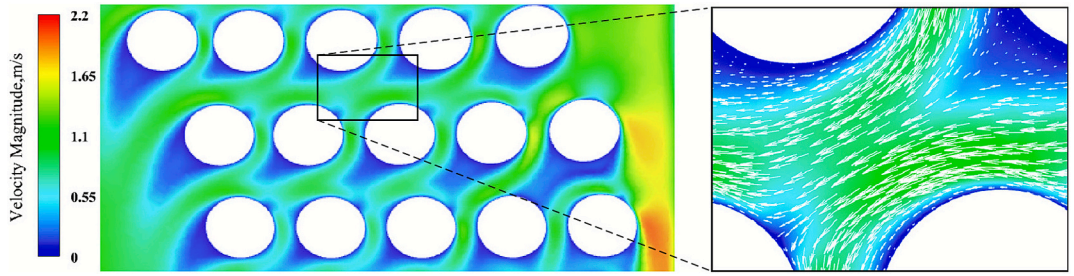

Fig. 18. Velocity contour and local vector in region C.

4.4.2. Pressure drop characteristics comparison

The pressure drop formula Δp is defined as follows (Jun and Xun-Ming, 2015):

$$\Delta p = Eu \cdot \frac{\rho u_{\max}^2 z}{2} \tag{2}$$

Average flow rate of minimum section of pipe row u:

$$u_{\max} = \frac{\sigma_1}{\sigma_1 - 1} \cdot u_{in} = \frac{S_1/D}{S_1/D - 1} \cdot u_{in} \tag{3}$$

Euler number, used to describe the characteristics of fluid flow. For different tube bundle arrangements (such as parallel arrangement and staggered arrangement), the Euler number calculation formula is different. In parallel arrangement, Eu is defined as:

$$Eu = \frac{(0.176 + 0.32\frac{\sigma_1}{c})}{\mathrm{Re}^{0.15}} \tag{4}$$

$$c = (\sigma_1 - 1)^{(0.43 + \frac{1.13}{\sigma_2})} \tag{5}$$

While in staggered arrangement, Eu is defined as:

$$Eu = \frac{(1 + \frac{0.47}{c})}{\mathrm{Re}^{0.16}} \tag{6}$$

$$c = (\sigma_1 - 1)^{1.08} \tag{7}$$

Row flow Reynolds number is defined as (Yangjia et al., 2023):

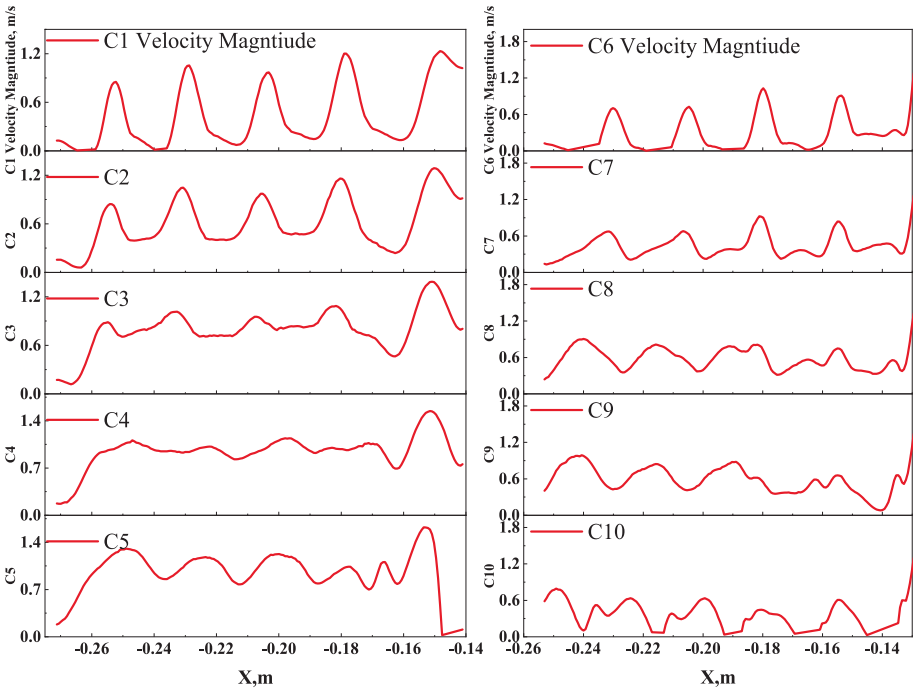

Fig. 19. Comparison of velocity distribution in region C.

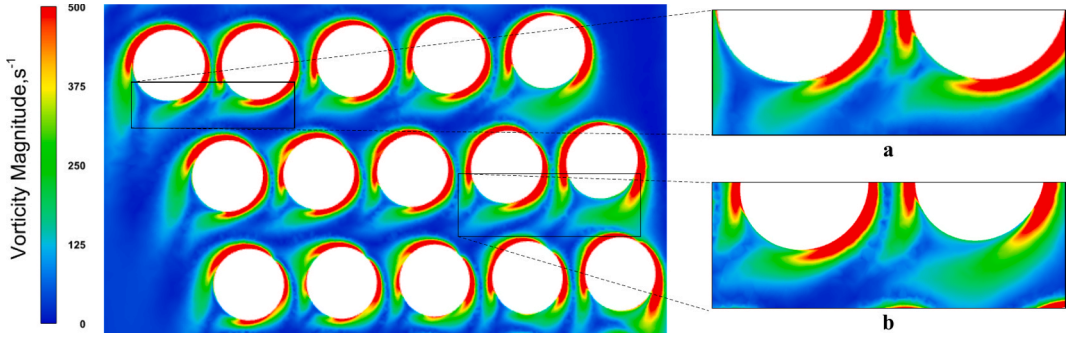

Fig. 20. Vorticity contour in region C.

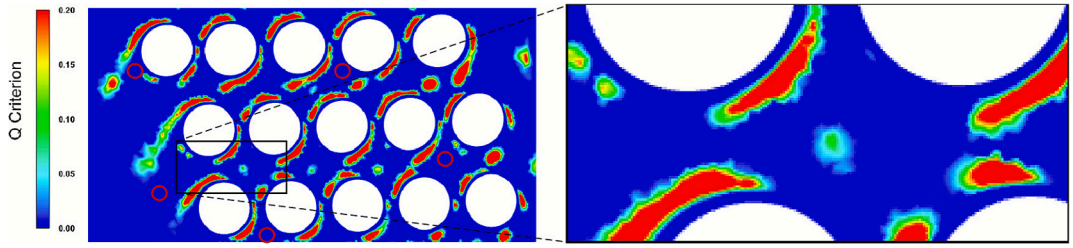

Fig. 21. Q criterion contour in region C.

$$\mathrm{Re} = \frac{\rho u_{\max} D}{\mu} \tag{8}$$

where is the Euler number and ρ is the density (kg/m^3); z is the number of tube rows along the flow direction, u_{in} is the average velocity of the minimum section of the tube rows;u_{max} is the air inlet speed (m/s); Re is Reynolds number, μ is dynamic viscosity (Pa·s), S1 is transverse tube spacing,S2 is longitudinal tube spacing (mm), as shown in Fig. 28; $\sigma_1 = S_1/D$ is transverse tube spacing ratio, $\sigma_2 = S_2/D$ is longitudinal tube spacing ratio, the values are shown in Table 2.

Based on the data shown in the table, the transverse spacing in the three Regions is basically consistent, and the longitudinal spacing varies, with Region B being larger than Region C, and Region C being larger than Region A. It indicates that the variable curvature helical structure mainly improves the fluid flow by changing the longitudinal spacing.

Based on the above formula, the pressure drop is calculated for different Regions, and the results are shown in the figure below:

$\Delta p_A = 0.671253\mathrm{Pa}$

$\Delta p_B = 1.156653\mathrm{Pa}$

$\Delta p_C = 0.785828 \sim 1.079054\mathrm{Pa}$

The higher pressure drop in Region B is the direct trade-off for this

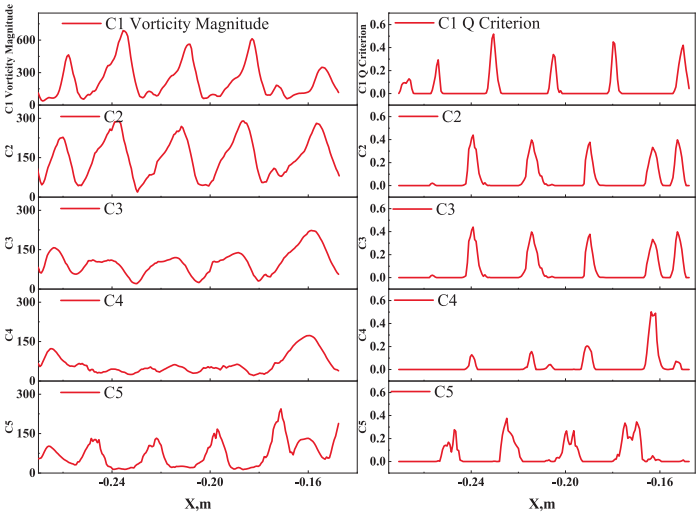

a. C1–C5

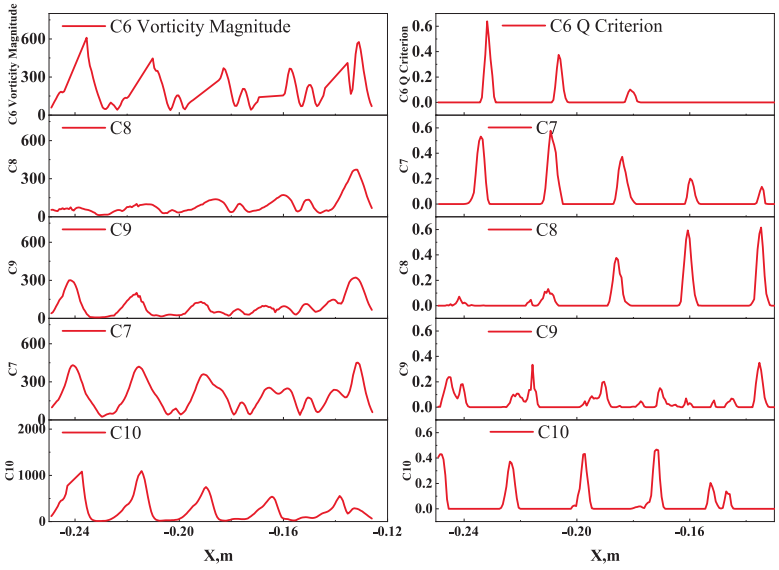

b. C6–C10

Fig. 22. Comparison of vorticity distribution (left) and Q criterion distribution (right) in region C.

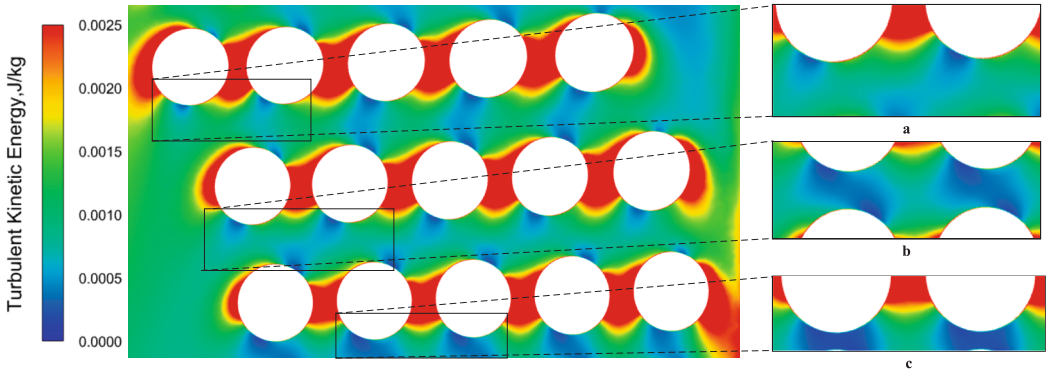

Fig. 23. Comparison of turbulence energy data in region C.

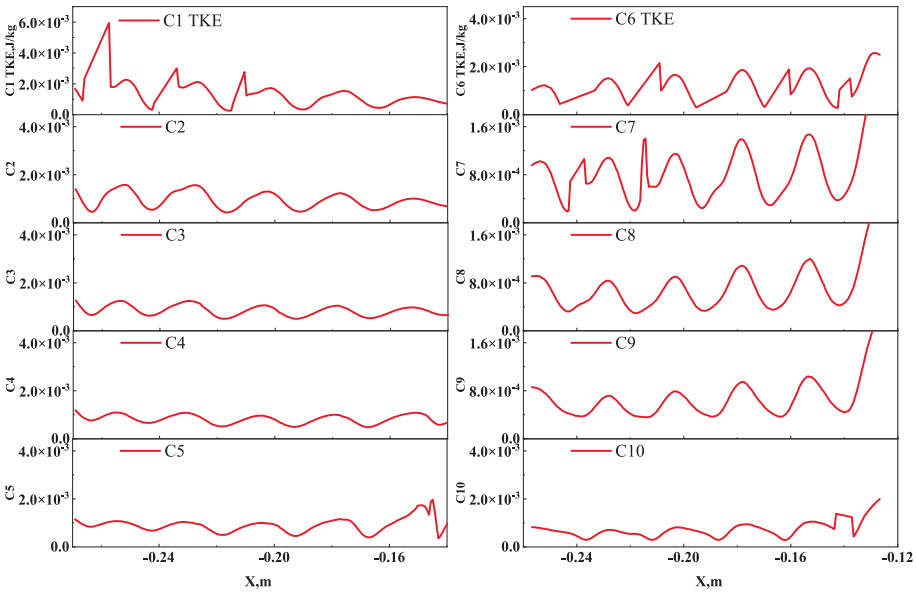

Fig. 24. Comparison of turbulent kinetic energy in region C.

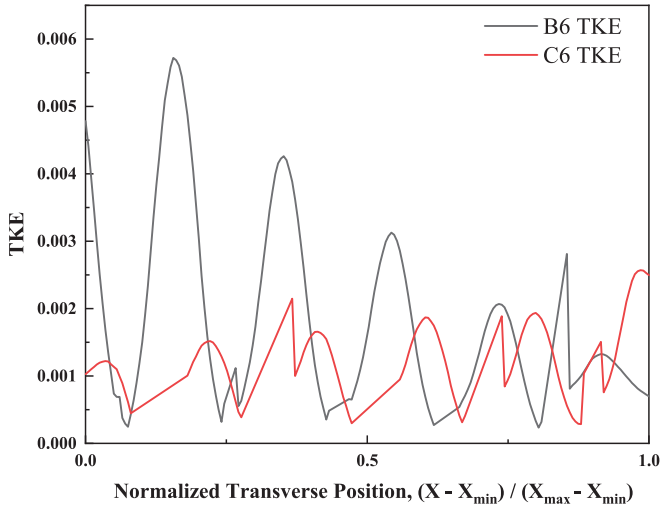

Fig. 25. Direct comparison of turbulent kinetic energy (TKE) profiles at downstream locations B6 (staggered arrangement) and C6 (hybrid arrangement). The transverse position is normalized by the local channel width.

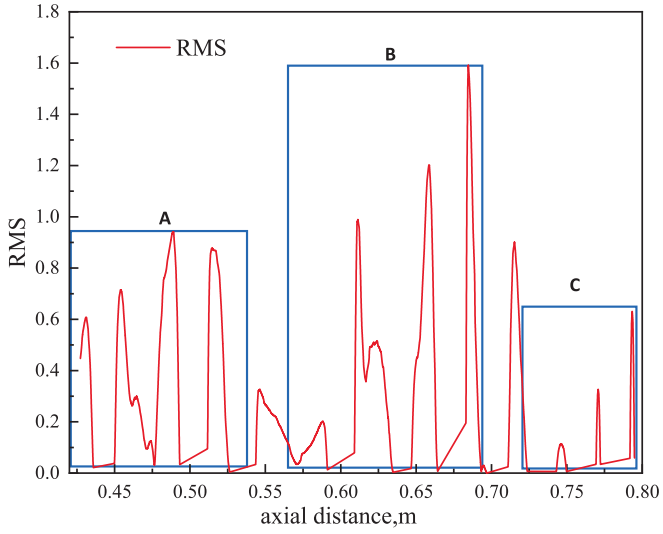

Fig. 26. Distribution of helium flow with axial height variation (along a single axis traversing three regions).

enhanced mixing. The energy expended to create and shed these intense vortices manifests as an irreversible pressure loss. This illustrates the classic compromise between heat transfer enhancement and pumping power in thermal design (Fig. 28, Table 3).

4.4.3. Heat transfer characteristics comparison

To evaluate the engineering heat transfer performance of staggered tube bundles with variable curvature, this study was carried out under constant heat flux (q = 10,000 W/m^2). The key parameters were: inlet velocity u_{in} = 0.5 m/s, pipe diameter D = 19 mm, fluid thermal conductivityλ = 0.16 W/(m).The calculation method refers to the heat transfer model of cross-swept tube bundle by Qin Yangjia et al. (Yangjia et al., 2023).

The Nusselt number (Nu) is used as a dimensionless parameter to quantify convective heat transfer intensity. Heat transfer efficiency is directly reflected by Nu value. It is defined as follows:

$$Nu = \frac{hD}{\lambda} = \frac{q}{\Delta T_{lm}} \cdot \frac{D}{\lambda}$$

The logarithmic mean temperature difference formula (ΔT_{lm})is presented as follows:

$$\Delta T_{lm} = \frac{T_{out} - T_{in}}{\ln[(T_w - T_{in})/(T_w - T_{out})]}$$

Region B achieved the highest Nusselt number (Nu = 7.16), significantly outperforming both Region A (Nu = 4.16) and Region C (Nu = 6.55). This represents a substantial 72 % enhancement over Region A and a 9.3 % improvement over Region C (Table 4). The superior thermal performance in Region B is a direct consequence of the flow dynamics detailed in Sections 4.2.1–4.2.3. It is noteworthy that although Region C exhibits a more uniform temperature distribution on the constant-Y plane (Fig. 29), indicative of good lateral mixing, its overall Nusselt number remains lower than that of Region B. This apparent contradiction highlights the critical distinction between the uniformity of the temperature field and the intensity of the local heat transfer process. The higher Nu in Region B is attributed to its stronger vortical structures and elevated turbulence levels (TKE), which aggressively thin the thermal

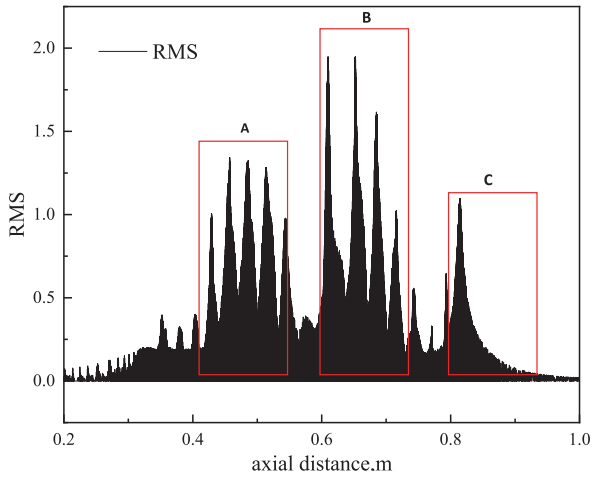

Fig. 27. Distribution of helium flow with axial height variation throughout the computational domain.

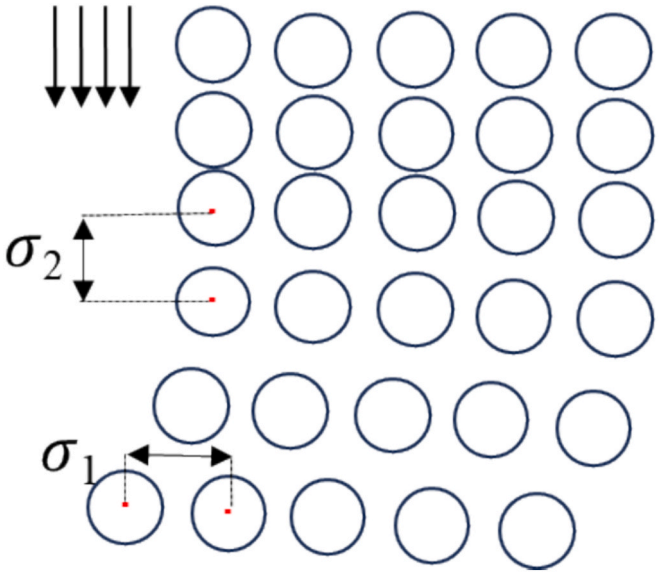

Fig. 28. Parameter diagram.

boundary layer at the tube surfaces. In contrast, Region C, while achieving better global thermal uniformity through moderate mixing, lacks the same intensity of small-scale, vortex-driven turbulence. Consequently, the convective heat transfer at the tube surfaces in Region C is less intense, resulting in a thicker average thermal boundary layer and a lower overall Nusselt number. Furthermore, the elevated and well-distributed turbulent kinetic energy (Fig. 17) ensures efficient macroscopic mixing of the coolant, minimizing local hot spots and leading to the more uniform temperature profile visualized in Fig. 29. In contrast, the suppressed vorticity and lower TKE in Region A result in a thicker thermal boundary layer and poorer mixing, explaining its lowest Nu value. Region C's intermediate performance is consistent with its hybrid flow structure, which exhibits moderate turbulence enhancement but lacks the coherent, high-energy vortices of the fully staggered region.

5. Conclusion

In the present study, multi-layer helical coil bundles arranged in longitudinal crossover with continuous periodic variation in outer curvature were proposed. Numerical simulation on the outside flow field in the shell-side of five-layer helical coil bundle was carried out. The flow field characteristics, including velocity and pressure distribution, vorticity and Q criterion, and turbulent kinetic energy were analyzed. The following conclusions were drawn:

(1) There are three typical Regions in the shell-side of multi-layer helical coil bundle, i.e. the in-line arrangement Region A, staggered arrangement Region B, and mixed arrangement Region C.
(2) In Region A, strong vortices were observed despite obstructions, and the alleviation of these obstructions was achieved, resulting in moderate heat transfer enhancement. In Region B, flow field perturbation was observed, and significant improvements in heat transfer efficiency were recorded, as indicated by the highest Nusselt number (Nu) measured in this region. Specifically, the Nusselt number in Region B was found to be 7.16, which was approximately 72 % higher than that in Region A (Nu = 4.16). This substantial increase underscored the substantial thermal enhancement facilitated by the staggered structure. In Region C, further elevation of both flow disturbance and heat transfer efficiency was noted, with a Nusselt number of 6.55, exceeding that observed in Region A by approximately 57 %. The key

Table 4
Nusselt numbers in different regions (constant heat flux).

Region	T_{lm} (K)	Nu
A	285	4.16
B	166	7.16
C	181	6.55

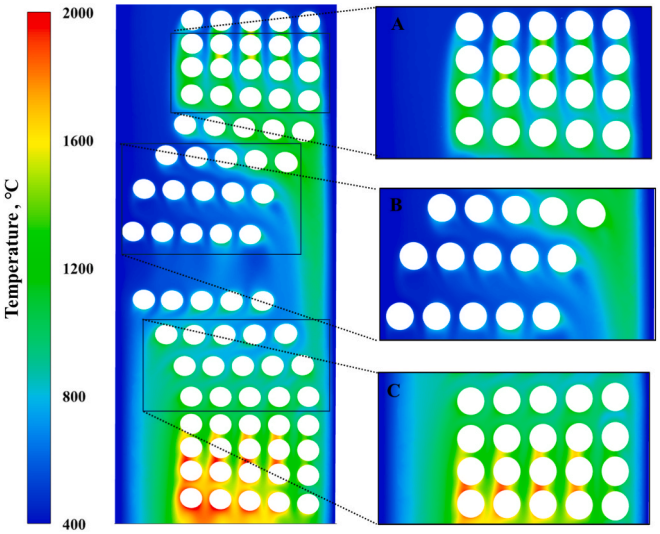

Fig. 29. Temperature distribution contour of the Y = 0 (constant heat flux).

Table 3
Parameter table.

Region	S_1 (mm)	S_2 (mm)	σ_1	σ_2	u_{max}(m/s)	ρ(kg/m^3)	μ(Pa·s)	u_{in}(m/s)
A	25.0	25.7 g	1.32	1.55	2.09	0.613	1.99×10^{-5}	0.500
B	25.1	41.1	1.32	2.07	2.079			
C	21.0	30.1	1.32	1.54	2.06			

mechanism for the superior performance in Region B was identified as the intense turbulent mixing driven by periodic vortex shedding and the consequent thinning of the thermal boundary layer.

(3) In conclusion, this study demonstrates that beyond mere geometric rearrangement, the active manipulation of flow physics through variable curvature and staggered bundling is key to enhancing shell-side performance. The primary mechanism is the promotion of large-scale, periodic vortical structures that disrupt the thermal boundary layer and promote intense turbulent mixing. The identified flow regimes (A, B, C) provide a blueprint for designers: Region A for low-flow-resistance applications, Region B for high-efficiency requirements, and Region C for a balanced compromise.

These findings provide experimental evidence for the design of helical coil bundles with tailored curvature profiles to maximize heat transfer performance. Future work should focus on the optimization of geometric parameters and the evaluation of pressure drop characteristics to achieve comprehensive thermal–hydraulic efficiency.

CRediT authorship contribution statement

Zhao Xijun: Conceptualization, Data curation, Formal analysis, Funding acquisition, Investigation, Methodology, Software, Validation, Visualization, Writing – original draft. **Qin Kaiwen:** Data curation, Funding acquisition, Methodology, Project administration, Resources, Supervision, Writing – review & editing. **Tang Xiaobin:** Validation, Supervision, Writing – review & editing.

Declaration of competing interest

The authors declare that they have no known competing financial interests or personal relationships that could have appeared to influence the work reported in this paper.

Acknowledgments

This work was supported by Project supported by the National Natural Science Foundation of China (Grant No. 12575362), the Graduate Research Innovation Program Project of NUAA (Grant No. xcxjh20240611), the Graduate Research Innovation Program Project of Jiangsu Province (Grant No. KYCX24_0617).

Data availability

Data will be made available on request.

References

Al-Hasan, M., Al-Odat, M.Q., Al-Busoul, M., 2012. An experimental investigation of forced convection heat transfer from a coiled heat exchanger embedded in a packed bed. Exp. Heat Transf. 25 (4), 363–376.

Asian, E., 2016. Numerical investigation of the heat transfer and pressure drop on tube bundle support plates for inline and staggered arrangements. Prog. Comput. Fluid Dyn. 1 (16), 38–47.

Beale, S.B., Spalding, D.B., 1999. A numerical study of unsteady fluid flow in in-line and staggered tube banks. J. Fluids Struct. 13, 723–754.

Bishara, F., 2013. Heat transfer enhancement due to swirl effects in oval tubes twisted about their longitudinal axis. J. Enhanced Heat Transf. 20 (4), 289–304.

Ding Xueyou, WenQinglong, Chen Zhiqiang, et al. Modeling of Thermal Hydraulic Characteristics for a LBE-Cooled Fast Reactor Helical Coiled Type Steam Generator [C]//. Proceedings of the 2020 International Conference on Nuclear Engineering, Virtual, Online, 2020: 21-26.

Gharbi, N.E., Kheiri, A., Ganaoui, M.E., et al., 2015. Numerical optimization of heat exchangers with circular and non-circular shapes. Case Stud. Therm. Eng. 6 (C), 194–203.

Herchang, A.Y., Jang, J., Yeh, J., 2002. Local heat transfer measurements of plate finned-tube heat exchangers by infrared thermography. Int. J. Heat Mass Transf. 45 (20), 4069–4078.

Hongfang, Gu., Dan, S., Yanmou, Z., et al., 2000. Research on enhanced condensation outside the horizontal coil tube with V grooves. Chem. Eng. Technol. 28 (5), 18–20.

Jiang, B., Liu, J., Liu, F., et al., 2019. Experimental study on effect of tube arrangement mode on heat transfer characteristics of a new type of elastic tube bundle. J. Phys. Conf. Ser. 1300 (1), 12021.

Jun, G., Xun-Ming, Z., 2015. Numerical simulation of convection heat transfer across spiral tube bundle. J. Therm. Sci. Technol. 5, 376–380.

Kunwer, R., Pandey, S., Sureshchandra, B.S., 2020. Comparison of selected shell and tube heat exchangers with segmental and helical baffles. Therm. Sci. Eng. Prog. 20, 100712.

Kwak, K.M., Torii, K., Nishino, K., 2003. Heat transfer and pressure loss penalty for the number of tube rows of staggered finned-tube bundles with a single transverse row of winglets. Int. J. Heat Mass Transf. 46 (1), 175–180.

Lee, S.J., Hassan, Y.A., 2020. Numerical investigation of helical coil tube bundle in turbulent cross flow using large eddy simulation. Int. J. Heat Fluid Flow 82.

Linkai, W., 2017. Study on numerical optimization of tube bundles arrangement for condensation heat transfer. School Energy Power Mech. Eng.

Markus Esch, A.H.D.K., 2012. Analysis of the influence of different heat transfer correlations for HTR helical coil tube bundle steam generators with the system code TRACE. Nucl. Eng. Des. 251, 374–380.

Menter, R.F. 1994. Two-equation eddy-viscosity turbulence models for engineering applications. 32(8), 1598-1605.

Miao Gui, Q.B.Y.G. 2016. Experimental study on the heat transfer enhancement by the combination of transverse groove tube and twisted tape inserts[C]. Proceedings of the ASME 2016 Power Conference, Charlotte, North Carolina.

Moawed, M., 2011. Experimental study of forced convection from helical coiled tubes with different parameters. Energy Convers. Manage. 52 (2), 1150–1156.

Moreno, A., Sparrow, E. Heat transfer, pressure drop, and fluid flow patterns in yawed tube bank. Heat Mass Transf. (30) 1979-1995.

Mori, Y., 1967. Study on forced convective heat transfer in curved pipes. Int. J. Heat Mass Transf. 1 (10), 37–59.

Mori, Y., Nakayama, W., 1967. Study on forced convective heat transfer in curved pipes, (part III: theoretical analysis under the condition of uniform wall temperature and practical formulae). Int. J. Heat Mass Transf. 5 (10), 681–695.

Namhyeong Kima, H.K.C.J., 2020. One-dimensional design approach to integrated steam generator with helical-coil tube bundles for a sodium-cooled fast reactor. Nucl. Eng. Des. 361, 100554.

Nianben, Z., Peng, L., Feng, S., et al., 2017. Turbulent flow and heat transfer enhancement in a heat exchanger tube fitted with novel discrete inclined grooves. Int. J. Therm. Sci. 111, 289–300.

Paul, S.S., Tachie, M.F., Ormiston, S.J., 2007. Experimental study of turbulent cross-flow in a staggered tube bundle using particle image velocimetry. Int. J. Heat Fluid Flow 28 (3), 441–453.

Qizhen, Y., 2015. Development and prospect of nuclear power and nuclear energy industry in China. Southern Energy Constr. 2 (04), 18–21.

Rivas, E., Rojas, E., 2016. Heat transfer correlation between Molten salts and helical-coil tube bundle steam generator. Int. J. Heat Mass Transf. 93, 500–512.

Ünal, U.U.O., Atlar, M., Gören, Ö., 2010. Effect of turbulence modelling on the computation of the near-wake flow of a circular cylinder. Ocean Eng. 37 (4), 387–399.

Wang, D., Alsenani, T.R., Singh, P.K., et al., 2023. A comprehensive numerical study on the fluid flow, thermal and exergetic performance of longitudinally ribbed spirally coiled tube with various shapes. Case Stud. Therm. Eng. 49, 103320.

Wang, H., Tao, T., Mei, X., et al., 2021. Experimental study on condensation heat transfer characteristics inside an inclined wave-finned flat tube of direct air-cooling system. J. Therm. Sci. 30 (2), 432–440.

Wei, Z., Jingsong, L., Huilie, S., et al., 2022. Thermal-hydraulic performance analysis of horizontal spiral tube steam generator for European lead-cooled fast reactor. Nucl. Power Eng. 3 (43), 38–45.

Yangjia, Q., Laihe, Z., Qihang, L., et al., 2023. Numerical investigation on heat transfer characteristics of staggered tube bundles in cross flow. J. Aerospace Power 38 (11), 2718–2728.

Yildiz, M.A., Merzari, E., Hassan, Y.A. 2018. Large Eddy Simulation of 5-Tube Bundle Helical Coil Steam Generator Test Section[C]. 26th International Conference on Nuclear Engineering, London, England.

Yoo Geun-Jong, C.H.D.W., 2012. Fluid flow and heat transfer characteristics of spiral coiled tube: effects of Reynolds number and curvature ratio. J. Cent. South Univ. 19, 471–476.

Zhao, Z., Che, D., 2012. Influence of tube arrangement on the thermal hydraulic performance of a membrane helical-coil heat exchanger. Numer. Heat Transf. Part A, Appl. 62 (7), 565–588.

Zhuang Nailiang, Tang Xiaobing, YangChenhao. A Steam Generator Helical Coil Assembly with Variable Curvature Wrapping: ZL202110692525.6.[P].